



Impacts of maximum snow albedo and land cover changes on meteorological variables during winter in northeast China

Donglei Fu ^{a,b}, Wei Zhang ^c, Yanfeng Xing ^d, Haizhi Li ^d, Pengjie Wang ^d, Bo Li ^{a,b}, Xiaofei Shi ^{a,b}, Jinxiang Zuo ^{a,b}, Stephen Yabo ^{a,b}, Samit Thapa ^{a,b}, Lu Lu ^{a,b}, Hong Qi ^{a,b,*}, Jianmin Ma ^{e,*}

^a School of Environment, Harbin Institute of Technology, Harbin, China

^b State Key Laboratory of Urban Water Resource and Environment, Harbin Institute of Technology, Harbin, China

^c School of Computer Science and Technology, Harbin Institute of Technology, Harbin, China

^d Heilongjiang Provincial Environmental Monitoring Center Station, Harbin, China

^e College of Urban and Environmental Sciences, Peking University, Beijing, China

ARTICLE INFO

Keywords:

Maximum snow albedo
Land cover
Anthropogenic heat
WRF
Dataset updating

ABSTRACT

The meteorological conditions in northeast China exhibit particular characteristics associated with snow cover in winter and dramatic land cover transformations. In this study, the Weather Research and Forecasting Model (WRF) is used to assess the influences of snow albedo and land cover changes on wind speed, temperature, relative humidity, and planetary boundary layer height (PBLH). Two new static geographical datasets, a maximum snow albedo dataset (MSA) developed by Beijing Normal University (BNU_MSA) and a land cover dataset developed by Tsinghua University (TU_LC), are employed for updating previous datasets in WRF. Besides, a case study for local anthropogenic heat (AH) parameters is conducted to examine its influences on temperature in winter. Modeled scenarios for 13 December 2017 to 15 January 2018 show that TU_LC yields a lower mean absolute error of 0.55 m/s for simulated wind speed, suggesting the usefulness of the TU_LC in modeled 10-m wind speed. The change in the wind speed is closely related to land cover transformations occurring over urban and forest regions. The spatially varying temperature agrees well with changes in the MSA. Simulation with updated AH parameters induces higher temperature over downtown Harbin and Changchun. Increasing PBLH is observed as compared with that using default datasets because of increasing temperature and heat fluxes induced by the decreases in MSA. The maximum differences of the wind speed and temperature between updated and default datasets in the vertical direction are confined within 600-m height above the ground surface.

1. Introduction

The land surface presents different features from local to global scales, which play important roles in temporal-spatial variations of meteorology (Chen and Dudhia, 2001; De Meij and Vinuesa, 2014; Zhu et al., 2017; Azhdari et al., 2018). These surface features, most importantly by land cover, topology, soil texture, and surface albedo, determine heat, moisture, momentum, and dust interactions between the land surface and overlying atmosphere at the microscale or mesoscale (Betts et al., 1996; DuVivier and Cassano, 2013; Tao et al., 2013; Srinivas et al., 2015). Therefore, these features are critical in the modeling of meteorological conditions over land surfaces and the upper air system (Kumar et al., 2008; Lee et al., 2016; Li et al., 2017; Fang et al., 2018; Massad et al., 2019).

The Weather Research and Forecasting (WRF) model is commonly used to perform weather forecast and to exploit meteorology variation. It contains a series of different geographical static datasets. Unfortunately, almost all these datasets with different resolutions are out of date and present lower precision in China and thus fail to capture updated features of underlying surfaces (Sertel et al., 2010; Schicker et al., 2016). While efforts have been made to incorporate new datasets into WRF (De Meij et al., 2015; Kurkowski et al., 2003; Li et al., 2018a), these updated datasets are not sufficient to address all significant changes in land surfaces. Encountering this problem, new datasets derived from the latest remote sensing image by the scientific communities are compiled to provide upgraded land cover, vegetation, topology, soil texture, and albedo. These datasets are localized and very appropriate for modeling (Trlica et al., 2017). Among them, more attention is paid to land cover

* Corresponding authors.

E-mail addresses: hongqi@hit.edu.cn (H. Qi), jianminma@lzu.edu.cn (J. Ma).

updating (Acs et al., 2014; Jimenez-Esteve et al., 2018; Thomas et al., 2018; Ooi et al., 2019). Besides, land surface parameters like albedo, surface emissivity, surface roughness, and soil moisture, often play important roles in the prediction of the air temperature, wind speed, and precipitation (Wen et al., 2012; Cermak et al., 2017; Toure et al., 2019).

In this paper, the study area covers the “Harbin-Changchun megalopolis” which is located in northeast China and entitled in 2013. In recent years, land cover transformations are being dramatic, inducing changes in land surface conditions, and exerting great effects on the atmospheric environment. Against this background, studies had proved that land cover change resulted in surface air temperature variation over or adjacent to this area (Wang et al., 2015; Liu et al., 2017). Land cover changes are so significant that the old datasets are unable to match covered features in reality. For example, noticeable disagreements of urban and built-up land and forest involved categories between these old datasets and realistic covers are readily discerned.

On the other hand, in winter, the snow-covered period lasts for almost 5 months from November to March next year, which is consistent with the results simulated by default datasets. 80% area of the model domain is covered by snow, 10.3% higher than that by prescribed datasets. Due to these features, it is interesting to investigate the effect of the new snow features on the meteorological conditions. Studies involving in winter snow based on observation approach have been proven that the snow properties can have impacts on air temperature, relative humidity, albedo, and heat fluxes in northeast China, inducing changes in the atmospheric environment and climate evolution (Li et al., 2017; Fu et al., 2019). In terms of modeling exercises in northeast China, Yu et al. (2017) found that well-presented snow cover could improve temperature prediction by 10%. Wang et al. (2011) proved that the WRF model was competent to simulate extreme snowfall events. However, as an important snow physics parameter, the effect of the maximum snow albedo (hereafter referred to as MSA) has not been explored in this region. In recent years, MSA exhibited differences as compared with the WRF’s newest MAXSNOALB_MODIS dataset (a default MSA dataset, for the period February 2000–July 2004) which was developed by Barlage et al. (2005). The measured monthly mean precipitation during winter (November ~ March next year) over 2000–2004 and 2016–2018 was 6.6 mm/month and 9.4 mm/month within the study area, respectively, which altered snow depth, snow equivalent water, and snow cover fraction. These in turn affected snow albedo (Chen and Dudhia, 2001; Qian et al., 2009; Oaida et al., 2015). Here, the WRF model is employed, it can provide an opportunity to investigate the changes in meteorological variables resulted from changed land cover and MSA on a large scale, which is the first goal of this study.

“Harbin-Changchun megalopolis” is known as an old industrial base in China. As the presence of heavy atmosphere pollution in winter, an inter-regional prevention and control project is being implemented by Harbin and Changchun. Both of the two cities had subjected to strict emission reduction from 2016 to 2018. However, air condition had not been further improved, which might be ascribed to unfavorable weather conditions. Land cover and maximum snow albedo changes exert great effects on wind speed, temperature, relative humidity, and planetary boundary layer height (Hirsch et al., 2014; Santos-Alamillos et al., 2015; Touchei et al., 2016). These variables play important roles in the haze formation as emission reduction in winter. Therefore, the precision of these meteorological variables should be ensured in modeling runs. To this end, we implemented two new datasets into our modeling exercises, these are a maximum snow albedo dataset re-processed by GLASS production developed by Beijing Normal University (hereafter referred to as BNU_MSA) and a land cover dataset derived from Tsinghua University (hereafter referred to as TU_LC). The modeled meteorological variables from the two datasets and default datasets are compared, to evaluate whether those target variables will be improved, which is the second goal of this study.

As the energy production and consumption are dominated by coal, a high level of anthropogenic heat (AH) emission induced by heavy

industry and central heating in winter is found over “Harbin-Changchun megalopolis”, which differs considerably from the South China in the wintertime (Zhu et al., 2017). AH released from cities significantly impacts local meteorological variables subject to the urban canopy model (Liao et al., 2014). Here, the response of the temperature variation to AH is quantified as associated with urban expansion in this study via a case study with local AH parameters. The results provide an insight into understanding for how and to what extent the natural elements (MSA) and anthropogenic disturbance (land cover transformation and winter heating) would otherwise alter meteorological variables.

2. Methods and data

2.1. Study area

The study area is located in northeast China ($123.55^{\circ}\text{E} \sim 128.68^{\circ}\text{E}$, $43.02^{\circ}\text{N} \sim 47.54^{\circ}\text{N}$), covering an area of $190,710\text{ km}^2$ and eight cities (Harbin, Daqing, Qiqihar, Suihua, Changchun, Jilin, Siping, Songyuan). The population in these cities is 39 million. This area generally is featured by flat terrain with a mean height of 228 m above the sea level. As one of the cold regions in China, the mean winter temperature is -10.9°C , and it may last for five months with snow cover. In 2013, the “Harbin-Changchun megalopolis” project containing 11 cities was initiated by China’s State Council to speed up economic development. Due to rapid industrialization and urbanization under this project, the region has experienced dramatic land cover transformation, especially in urban areas and their surroundings.

2.2. WRF configuration

Simulations were carried out using the WRF-ARW (Advanced Research WRF) version 3.9.1 from 13 December 2017 to 15 January 2018 with triple two-way nested domains (Fig. 1) with the innermost domain on a 3-km resolution covering the majority of “Harbin-Changchun megalopolis”. The first two days were treated as spin-up time. The boundary and initial conditions used the data collected from the National Center for Environmental Prediction (NCEP’s Global Final Analysis (FNL) with a horizontal resolution of 1° by 1° at 6-h interval. Following previous modeling studies over the Northeast China (Chen et al., 2014; Wen et al., 2014; Wang and Sun, 2018), five commonly used physics parameterization schemes, including Kain-Fritsch cumulus scheme (basically by the outermost domain), YSU boundary layer scheme, RRTM longwave scheme, Dudhia shortwave scheme, and Noah Land Surface Model, were adopted in our modeling exercises. The

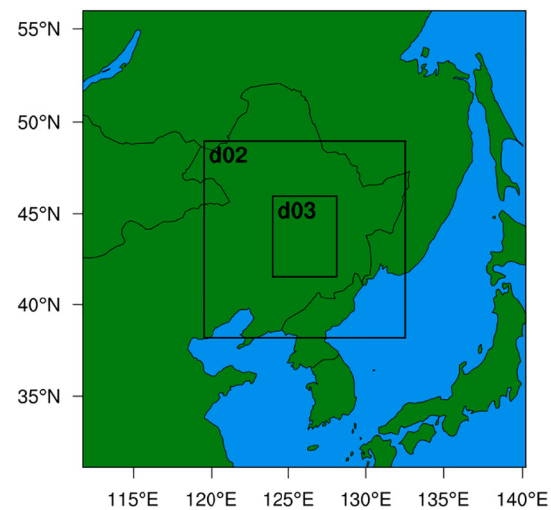


Fig. 1. Domains in this study. The 3-km resolution for the target innermost domain.

default parameters belonging to these schemes were used directly.

Urban canopy model (hereafter referred to as UCM) coupling with Noah LSM is prescribed in WRF. The urban and built-up land in the USGS land cover dataset (hereafter referred to as USGS_LC) needs to be reclassified into low-intensity residential (category 31 in USGS_LC), high-intensity residential (category 32 in USGS_LC), and industrial/commercial (category 33 in USGS_LC) in UCM. Here, high-intensity residential land cover is defined if the fraction of urban and built-up land category within a grid is equal to or greater than 30%. Otherwise, the land cover type is defined as low-intensity residential area (Kuik et al., 2016). For those industrial or commercial areas, the entire grid occupied by urban and built-up land is classified manually. It should be stated that the UCM is only applied to the innermost domain. Also, to our knowledge, UCM has not been adopted in the entire “Harbin-Changchun megalopolis”, therefore, it needs to be evaluated. These new datasets have high resolution and the Mosaic Approach with tiles number $N = 3$ is introduced to effectively maintain the sub-grid effect. In this study, both the objective and surface nudging to alleviate bias among simulations will not be applied.

2.3. Default datasets specification

The land cover default datasets prescribed in WRF include the USGS_LC (Loveland et al., 1995) and MODIS land cover dataset (hereafter referred to as MODIS_LC, Friedl et al., 2002). These two datasets created large extents of misrepresentation. For example, urban and built-up land and forest misrepresentations in USGS_LC (Schicker et al., 2016; Fang et al., 2018), forest and snow misrepresentations in MODIS_LC (Gao and Jia, 2013; Pan et al., 2017) have been reported. The accuracy of the MODIS_LC is evaluated to be 72.3–77.4% globally (Friedl et al., 2010), however, ranges from 31.86% to 58.65% across China (Yang et al., 2017). The USGS_LC is chosen as the default dataset because of its 49% accuracy increment (Gong, 2009) and the USGS_LC provides higher heterogeneity and more land categories. For default MSA datasets, the original old dataset (April 1985–December 1987, January 1989–March 1991) is replaced by the MAXSNOALB_MODIS dataset with 0.05° resolution produced by Barlage et al. (2005). The modeling results revealed significant changes generated in BNU_MSA over the study area, especially in urban and forest regions.

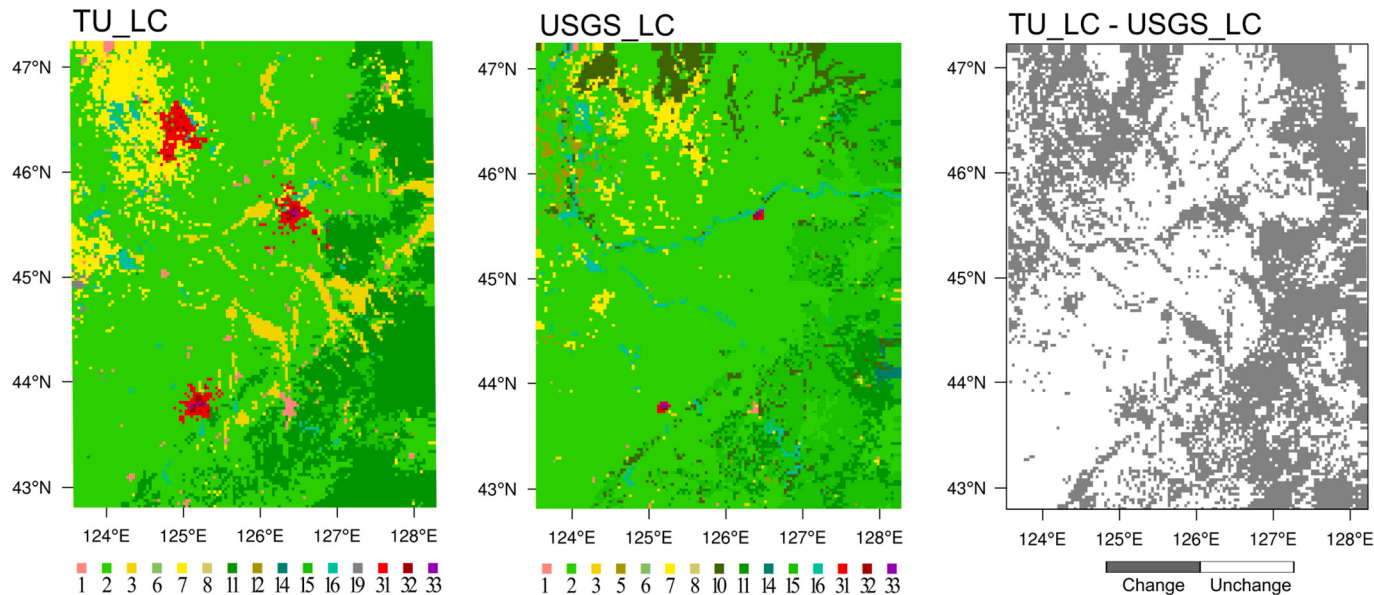


Fig. 2. Land cover datasets in this study. Left panel: TU_LC, mid-panel: USGS_LC, right panel: land cover transformations by the two datasets. Land cover categories: 1-Urban and Built-up Land, 2-Dryland Cropland and Pasture, 3-Irrigated Cropland and Pasture, 5-Cropland/Grassland Mosaic, 6-Cropland/Woodland Mosaic, 7-Grassland, 8-Shrubland, 10-Savanna, 11-Deciduous Broadleaf Forest, 12-Deciduous Needleleaf Forest, 14-Evergreen Needleleaf Forest, 15-Mixed Forest, 16-Water Bodies, 19-Barren or Sparsely Vegetated, 31-Low Intensity Residential, 32-High Intensity Residential, 33-Industrial or Commercial.

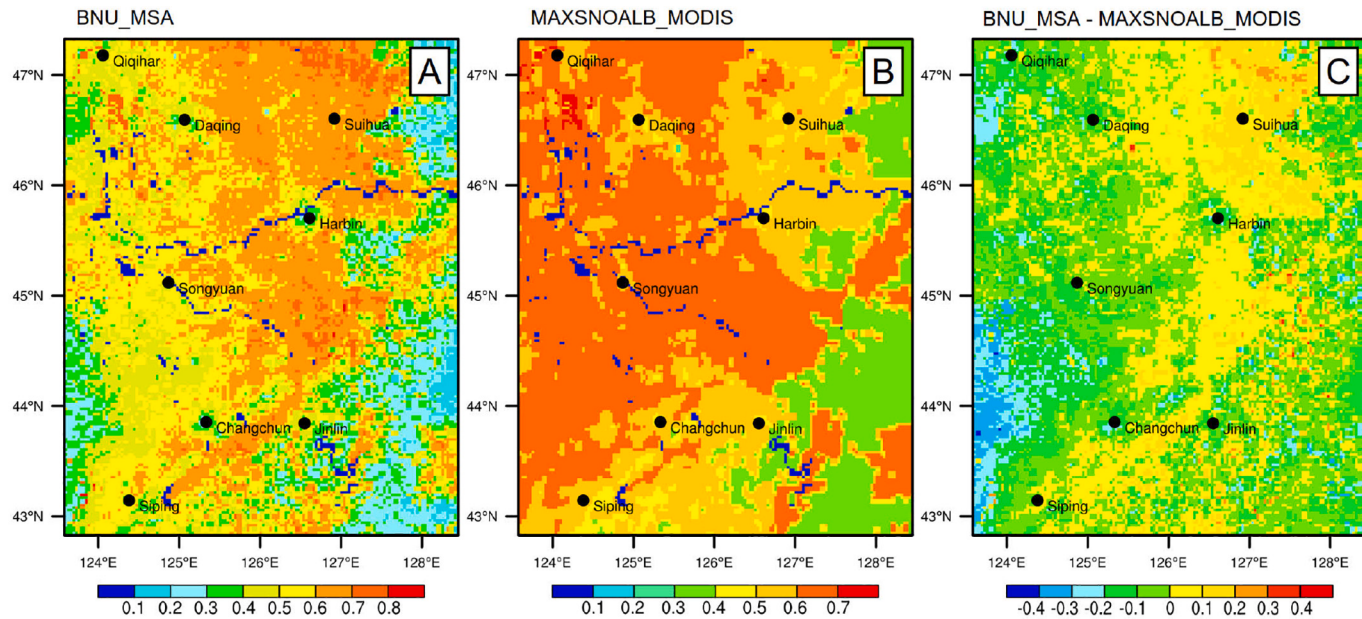


Fig. 3. Maximum snow albedo datasets. A- the new dataset BNU_MSA, B- the default dataset MAXSNOALB_MODIS, C- differences by BNU_MSA minus MAXSNOALB_MODIS. The black dot represents the city's relative position.

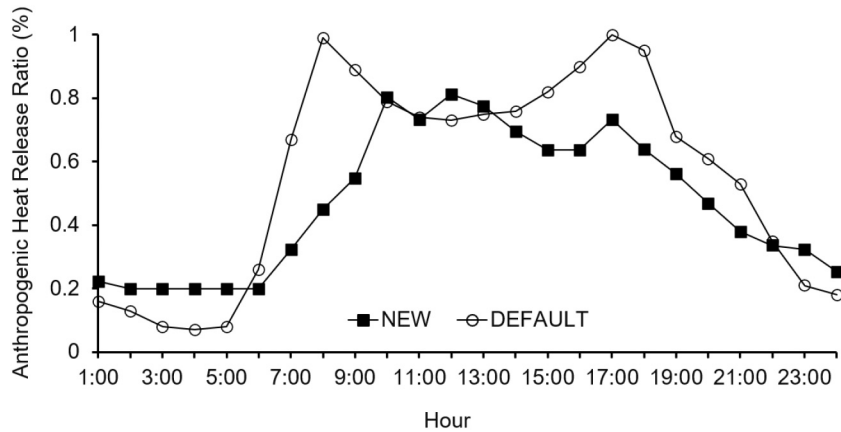


Fig. 4. The diurnal variation of AH release. NEW and DEFAULT represents modified and default AH Release Ratio, respectively.

Fig. 4 shows updated *Anthropogenic Heating Diurnal Profiles*.

2.5. Observational stations and data

Fig. 5 shows 40 met observational stations, two sounding stations, and a laser radar station across the model domain. 28 out of 40 met stations show a decrease in MSA. For the land cover category, mosaic distribution of DCP and LIR (or UBL) are found at 33 stations in TU_LC, however, most of them are fully occupied by DCP in USGS_LC.

Hourly data at these ground weather stations were collected from the China Meteorological Data Service Center (<http://data.cma.cn/>). Sounding data with 12-h interval (00:00 and 12:00) at Harbin and Changchun stations were derived from the University of Wyoming (<http://weather.uwyo.edu/upperair/seasia.html>). The boundary layer height data with a 20-min interval were provided by Heilongjiang Environmental Monitoring Center. Detailed information for these met stations can be referred to Table S1.

2.6. Model scenarios and evaluation metrics

Four model scenarios with default AH parameters were designated,

including maximum snow albedo modification (ALB), land cover modification (TU), combined land cover and maximum snow albedo modification (TUALB), and default datasets (WAT). TAAH and TADEF are used to explore the influence of AH on temperature through the two above-mentioned localized parameters in UCM (Table 1). It should be stated that the UCM is only applied to the innermost domain. These scenarios adopt identical initial conditions, lateral boundary conditions, and physics schemes. Simulations with the two new datasets with default UCM parameters (ALB, TU, TUALB) are referred to as the “updated simulations” hereafter.

The modeled land surface and near-surface wind speed (hereafter referred to as WS), temperature, and relative humidity (hereafter referred to as RH) subjected to the changes in MSA and land cover are evaluated against measurement data. The planetary boundary layer height (hereafter referred to as PBLH) is assessed by the single observational station. The modeled 10-m wind speed (hereafter referred to as WS10), 2-m air temperature (hereafter referred to as T2), and 2-m relative humidity (hereafter referred to as RH2) are verified against observation. BIAS is used to measure the deviation by comparison with observations. Mean absolute error (MAE) is used to evaluate the improvement of simulations. The Pearson correlation coefficient (CC)

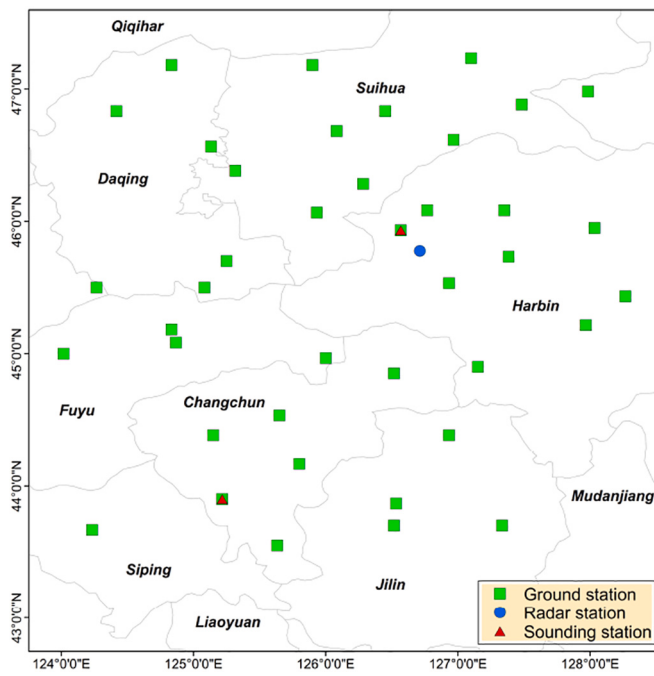


Fig. 5. Observational stations in the innermost domain. Green box-ground weather station, red triangle-sounding station, blue dot-laser radar station.

Table 1
Modeling scenarios.

Simulation	d01	d02, d03	AH
ALB	MAXSNOALB_MODIS	BNU_MSA	Default parameters
TU	TU_LC	TU_LC	Default parameters
TUALB	TU_LC + MAXSNOALB_MODIS	TU_LC + BNU_MSA	Default parameters
WAT	USGS_LC + MAXSNOALB_MODIS	USGS_LC + MAXSNOALB_MODIS	Default parameters
TAAH	TU_LC + MAXSNOALB_MODIS	TU_LC + BNU_MSA	Modified parameters
TADEF	TU_LC + MAXSNOALB_MODIS	TU_LC + BNU_MSA	Close

for correlation.

$$\text{BIAS} = \frac{1}{n} \sum_{i=1}^n (W_i - O_i)$$

$$\text{MAE} = \frac{1}{n} \sum_{i=1}^n |W_i - O_i|$$

$$\text{CC} = \frac{\sum_{i=1}^n (W_i - W_a)(O_i - O_a)}{\sqrt{\sum_{i=1}^n (W_i - W_a)^2(O_i - O_a)^2}}$$

wherein W_i and O_i represent modeled results and observations. W_a and O_a are on average. "n" is the frequency of extracted data.

3. Result

3.1. 10-m wind speed

Fig. 6(A) shows the mean MAE of WS10 from different model scenarios at met stations. Generally, MAE was 0.92 m/s and 0.91 m/s in ALB and WAT, respectively. Both TU and TUALB performed equally well with the same MAE of 0.55 m/s, demonstrating the usefulness of TU_LC in modeling WS10. Consistent improvement was discerned at those met stations within the urban regions except for Jilin. Modeled WS10 at 28 out of 32 met stations located in the suburb area showed varying degrees of improvement, which was partly attributable to more detailed surface features provided by TU_LC, such as the roughness length. Modeled WS10 with lower MAE around 0.4 m/s or less by TU and TUALB could be seen in the northeast and southwest of the model domain, where the wind speeds were often less than 3.0 m/s. Whereas, the wind speed greater than 3.8 m/s always exhibited higher MAE. The TU_LC nicely captures realistic land cover categories especially those over the urban regions, with a precision of 80% by validation with BIGEMAP (Table S2). It was found nineteen met stations experienced land cover transformations presenting higher improvement than the average, and well met with the observations. Besides, observed meteorological variables showed evolutions while referring to historical observations induced by land cover changes (Table S3).

Simulated and observed mean WS10 at 3-h interval averaged all met stations from 15 December 2017 to 15 January 2018 are shown in **Fig. 7(A)**. As shown, more than 80% periods from each model scenario were

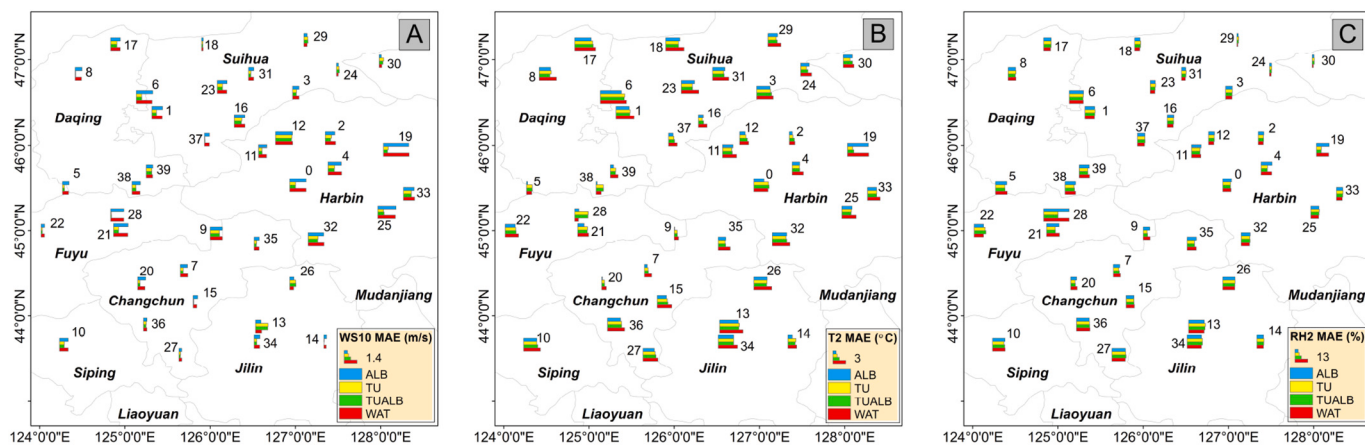


Fig. 6. Spatial histograms of MAE for simulated 10-m wind speed, 2-m air temperature, 2-m relative humidity. Word in bold-italicized font denotes city name. The station number is listed beside the histogram. 0-Acheng, 1-Anda, 2-Bayan, 3-Beilin, 4-Binxian, 5-Daan, 6-Daqing, 7-Dehui, 8-Dumeng, 9-Fuyu, 10-Gujiazi, 11-Harbin, 12-Hulan, 13-Jinlin, 14-Jiahe, 15-Jiutai, 16-Lanxi, 17-Lindian, 18-Mingshui, 19-Mulan, 20-Nongan, 21-Qianguo, 22-Qianan, 23-Qinggang, 24-Qinggan, 25-Shangzhi, 26-Shulan, 27-Shuangyang, 28-Songyuan, 29-Suiling, 30-Tieli, 31-Wangkui, 32-Wuchang, 33-Yanshou, 34-Yongji, 35-Yushu, 36-Changchun, 37-Zhaodong, 38-Zhaoyuan, 39-Zhaozhou.

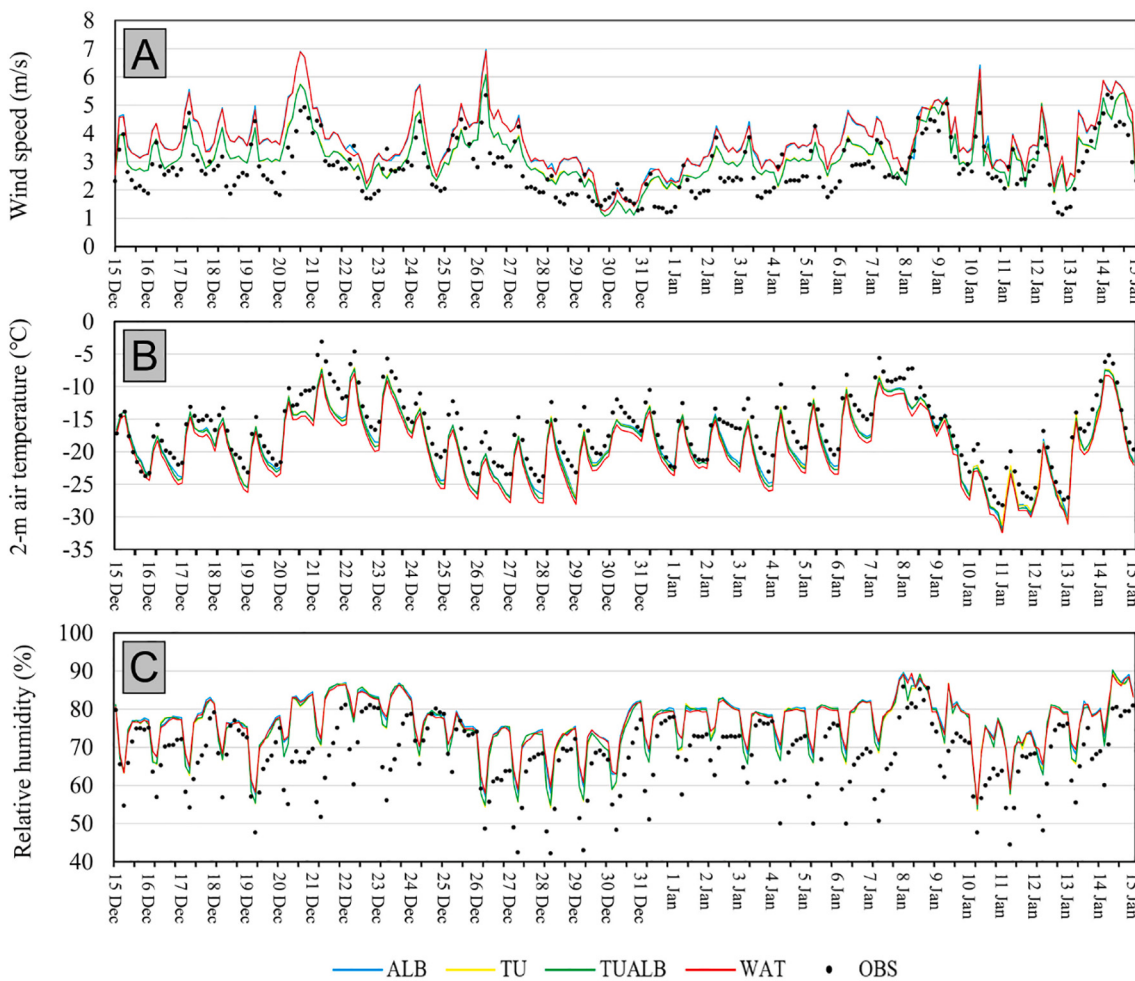


Fig. 7. Time series of simulated 10-m wind speed, 2-m air temperature, and 2-m relative humidity and observations from 15 December 2017 to 15 January 2018. ALB, TU, TUALB, and WAT (color lines) represent the four scenarios using default AH parameters in UCM, values are averaged by all met stations. OBS (black dots)-observational data.

overestimated as compared with measurements, with mean BIAS at 0.89 m/s (ALB-OBS), 0.37 m/s (TU-OBS), 0.37 m/s (TUALB-OBS), and 0.88 m/s (WAT-OBS), respectively. The daytime (00:00–06:00) mean BIAS of WS10 (0.51 m/s) from all scenarios were respective lower than that in the nocturnal cases (09:00–21:00, 0.75 m/s). This suggests that the mean WS10 fluctuation is liable to occur during the nighttime, in line with previous studies (Carvalho et al., 2012; Ioannidou et al., 2014). No significant differences in WS10 were identified between ALB and WAT. The WS10 in TU and TUALB were almost identical with lower MAE.

3.2. 2-m air temperature

3.2.1. The influence of new datasets on 2-m air temperature

The differences in the MAE for T2 are displayed in Fig. 6(B). As seen, the simulated T2 at the majority of met stations were improved by simulating with new datasets. The MAE in ALB, TU, TUALB, and WAT was 2.21 °C, 2.33 °C, 2.44 °C, and 3.11 °C, respectively, thus, with the lowest MAE, the MSA dataset was very useful in modeling T2. Modeled T2 performed differently at Mulan and Songyuan, where the modeled T2 improvement achieved by 3.68 °C (TU) by the former, while degraded by 2.49 °C (TUALB) for the latter. Those met stations located in urban regions also achieved improvements except for Songyuan, indicating that the new datasets are site-sensitive due to partitioning UBL fractions at a grid. The underlying surfaces were altered as urbanization happened, the T2 was underestimated for all scenarios except for 15

December (Fig. 7(B)), the BIAS was −2.16 °C (ALB), −2.29 °C (TU), −2.39 °C (TUALB), −3.07 °C (WAT), respectively, similar to Li et al. (2018b). Obviously, each simulation nicely agreed with observation and small gaps between them were observed, as shown in their respective high CC values (Table 2). This suggests that simulations do fairly well in reproducing the magnitudes and trends. On the other hand, simulations performed differently for the diurnal variation. Higher MAE always occurred in the daytime (2.61 °C) as compared with that in the nighttime (2.30 °C).

3.2.2. The influence of AH on 2-m air temperature

The AH prescribed in the UCM scheme was updated in this study. The effect by the TAAH generally performed better than TADEF. In specific, the modified parameters have more accurate surface heat representation which help enhancement not only temporal tendency but also improve the T2 performance by lower BIAS and MAE. T2 was still underestimated in TAAH but the BIAS and MAE dropped by 0.75 °C and 0.36 °C compared with TADEF, respectively (Fig. 8). Interestingly, it was found that the TAHC (mean values of Harbin and Changchun stations, the blue line in Fig. 8) indicated further improvement, the MAE dropped by a large extent of 0.9 °C, which indicated the sensitivity of large cities to the AH. Here, the Taylor diagram is used to provide a method of graphically summarizing how closely the simulated T2 against observation. The standardized deviation of T2 in met stations is averaged by city (Fig. 9). The Taylor diagram showed that the two simulations (TAAH, TADEF) agreed well with observations, but the TAAH, with

Table 2

Mean absolute error (MAE), bias (BIAS), and the Pearson correlation coefficient (CC) of simulated variables. WS10- wind speed at 10-m (m/s), T2- air temperature at 2-m ($^{\circ}$ C), RH2- relative humidity at 2-m (%), PBLH- planetary boundary layer height (m). ALB, TU, TUALB, and WAT- the four scenarios with default AH parameters in this study.

	MAE				BIAS				CC			
	WS10	T2	RH2	PBLH	WS10	T2	RH2	PBLH	WS10	T2	RH2	PBLH
ALB	0.92	2.21	9.14	89.94	0.89	-2.16	9.06	18.85	0.54	0.85	0.57	0.69
TU	0.55	2.33	8.32	112.67	0.37	-2.29	8.25	-67.38	0.53	0.88	0.62	0.58
TUALB	0.55	2.44	8.34	97.08	0.37	-2.39	8.28	-9.96	0.54	0.88	0.61	0.57
WAT	0.91	3.11	9.02	111.35	0.88	-3.07	8.96	-52.00	0.53	0.84	0.55	0.69

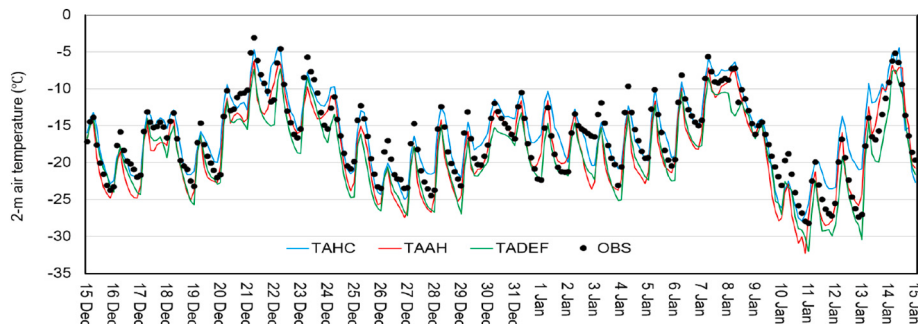


Fig. 8. Time series of simulated and observed 2-m air temperature from 15 December 2017 to 15 January 2018. TAHC- simulated mean 2-m air temperature of Harbin and Changchun stations with modified AH parameters. TAAH- simulated mean 2-m air temperature by all met stations with modified AH parameters. TADEF- simulated mean 2-m air temperature by all met stations with AH close. OBS- observational data.

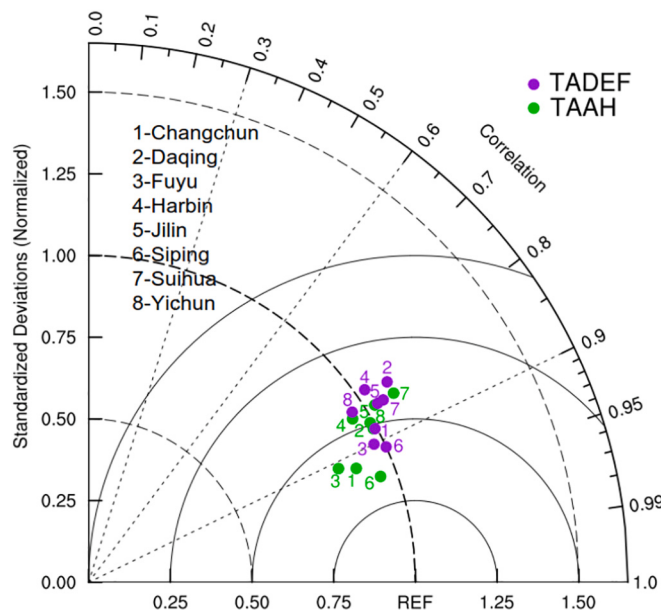


Fig. 9. Taylor diagram of mean 2-m air temperature. TAAH is represented by green dots and TADEF by purple dots. Value is averaged by city.

higher correlations and lower root-mean-square differences, performed better than TADEF.

3.3. 2-m relative humidity

Modeled RH2 is exhibited in Fig. 6(C). The MAE performed reductions from the southwest to the northeast across the modeled domain. Low MAE centralized over Suihua city, which could be as low as less than 1.9%. It is worth noting that, high MAE frequently occurred at those met stations within urban regions where Mosaic Approach and UCM are employed, which infers complex inducements in modeling RH2

in the urban region. The simulated effect in ALB represented degradation, therefore, the MSA exhibits limited impacts on RH2. For TU and TUALB, MAE respectively decreased by 0.70% and 0.68% on average, agreeing with Wen et al. (2014) over the same region, but these changes were still negligible in reality. RH2 was overestimated for most periods in contrast with observation (Fig. 7(C)), with BIAS of 9.06% (ALB), 8.25% (TU), 8.28% (TUALB), and 8.96% (WAT), respectively. Recall that land cover is seen as one of the key factors to determine water and moisture conditions, additionally, radiation variation induced by changed albedo has a close relationship with heat fluxes, however, no significant effects were found induced by them when the surface was covered by snow.

3.4. Planetary boundary layer height

Measured PBLH originated from an atmosphere detection laser radar possessed by Heilongjiang environmental monitoring station from 16 December to 5 January were collected. Large deviations between simulations were shown (Fig. 10), which indicates that PBLH is sensitive to new datasets. In specific, the maximum modeled PBLH for each period was always modeled in ALB or TUALB, while lower PBLH were frequently involved in TU and WAT cases. The reason for this may be due to generally low surface albedo in BNU_MSA, leading to temperature increase and more heat fluxes at the land surface. For modeling results, PBLH in ALB exhibited lower MAE, with 89.94 m on average.

3.5. Vertical profiles

Vertical profiles of WS, temperature, and RH at 00:00 and 12:00 local time (LST) on 2 January 2018 at Harbin and Changchun, extending from the surface to the 500-hPa, are shown in Fig. 11. In general, the simulated WS showed good agreement with the observations, particularly at 1000-hPa and 700-hPa at Changchun station (Fig. 11(G), Fig. 11(J)). The reason for this was that both TU_LC and USGS_LC created the same high-intensity residential category and thus shared the same surface roughness lengths. Deviations of simulated WS and temperature from the measurements could be seen at Harbin station within 900-hPa but

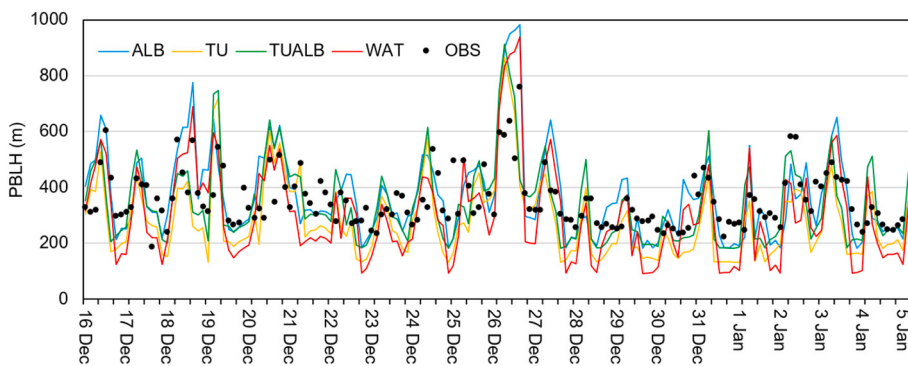


Fig. 10. Time series of simulated and observed PBLH from 16 December 2017 to 5 January 2018 at Harbin station.

relatively slight deviations above 700-hPa. Also, ALB, TU, and TUALB model scenarios yielded lower MAE of the two met variables below 900-hPa as compared with that in WAT. The large differences between modeled and measured RH were seen on the surface at the Harbin site and 900-hPa height at Changchun site at 00:00 LST.

4. Discussions

4.1. Evaluation of the two new datasets

In general, predicted WS10 and T2 were improved at most met stations, and slight improvement of modeled RH2 was achieved by TU and TUALB (Table 2). MSA and land cover experienced dramatic changes in the past years in the model domain. The albedo decreased at two-thirds of model grids across the study area. Land cover types at 40.8% grids had been switched into new categories. Fifteen DCP related transformations were also readily discerned, involving agricultural and forestry regionalization and urban development (Table S4). In addition, urban-related categories yielded a 1515 km² increment where the surface characteristics would be altered. For most observed stations, TU_LC outperformed USGS_LC in the WS10 simulation. ALB created the largest improvements for simulated T2 and PBLH (Table 2). As aforementioned, the improvements of modeled WS, temperature, and PBLH resulted from new datasets were proved by measured data. The performances of variables were detailed in a Taylor plot in Fig. S3.

As referring to the previous studies, the degrees of improvement of WS10 and T2 were in the range of 0.1–0.55 m/s and 0.1–0.95 °C after experiencing datasets incorporation (CLC, GLCC, MODIS, monthly surface albedo, etc.). The simulated WS10 and T2 with mean MAE of 0.36 m/s and 0.78 °C in this study outperformed most of them, which further indicated the adaptability and representativeness of TU_LC and BNU_MSA by capturing the land surface characteristics in reality to a large extent. Here, surface roughness length (SFZO) experienced varying degrees of variations in response to land cover transformation. Meteorological variables which are subject to varying SFZO will be discussed in the following sections.

4.2. Changes in wind speed

WS10 differences between “updated simulations” and WAT, defined by ALB-WAT, TU-WAT, and TUALB-WAT, are shown in Fig. 12. Fig. 13 illustrates the vertical cross sections of WS along with the innermost model domain as shown by the black line (Fig. 12(A)), and the same for subsequent temperature, RH, and PBLH. It should be noted that the black dot in the figure represents the relative position of the geometrical center for cities, rather than met observational stations. The sensitivity of WS10 to the changes in the SFZO will be evaluated.

The wind speed differences simulated by the two model scenarios ALB and WAT, defined by WS10_{ALB-WAT} (the same as the other differences) ranged from -0.13 m/s to 0.22 m/s with an average of 0.04 m/s

(Fig. 12(A)). The similar magnitudes were also observed in its vertical cross section occurred in Fig. 13(A). Hence, the updated MSA exerts a weak influence on wind speed, both horizontally and vertically, a similar result has been reported by Zahra and Hashem (2018). The significant impact of land cover transformation on WS10 was confined to the urban and water underlying surfaces, the former can be interpreted by the SFZO induced turbulent mixing when applying the UCM (Li et al., 2018c). For the latter, the SFZO remains the same during winter, which suggests the impact of water bodies involving transformations on WS10 is overestimated. Large values of WS_{TU-WAT} and WS_{TUALB-WAT} in the vertical direction were centralized over urban regions in Harbin (126.5° ~ 127.0°) and Changchun (125.1° ~ 125.5°), typically within the 600-m height (Fig. 13(B), Fig. 13(C)). The surface roughness lengths in the two new land cover datasets markedly differed from USGS_LC but presented more urban characteristics (Fig. 14), where stronger turbulences and fluxes could be observed in the near-surface layer (Jimenez et al., 2012; Tao et al., 2013).

4.3. Changes in temperature

Fig. 15 shows the T2 differences by simulations with new datasets minus WAT. As seen, for T2_{TU-WAT}, it increased in all city areas during the daytime except Songyuan and Jilin (Fig. 15(A)). However, it was featured by an overall decrease over most cities at night (Fig. 15(B)). The reason was that the change in roughness and albedo resulting from urbanization during daytime was discerned to contribute appreciably to radiation and heat flux changes. T2 is affected directly by the sensible heat flux (HFX) that is sensitive to land cover (Yu et al., 2012). Here, the HFX rose by 5.8 W/m² over urban region (Fig. S4), and thus T2. Coincidentally, the T2_{TUALB-WAT} exhibited similar features (Fig. 15(C)).

Interestingly, T2_{TU-WAT} scenario generally presented negative values when the transformation occurred between DCP and mixed forest in the right half of the study area, but positive in the T2_{TUALB-WAT} scenario. This is likely attributed to the changing surface albedo generated by the new MSA dataset, the region featured by increasing T2 always corresponded to a decreasing MSA, and vice versa, from which indicating that the albedo change instead of land cover transformation is of great sensitivity on T2 variation over forest region. The majority of met stations were subject to albedo and land cover variations but caught well with the reality, ameliorating heat fluxes, surface emissivity, and long-wave radiation, etc., by the new inputs in the atmospheric environment as the underlying surface covered by snow, thus, yielding to the modeling T2 improvement.

Concerning the impact of AH on T2, the MAE reduced by 0.36 °C from TAAH to TADEF. The improvement was due to characteristics of UCM land cover classifications as well as the modeling resolution, thus the majority of stations located in the suburb were classified into UBL instead of the three new categories in UCM. It was found that the majority of downtown Harbin and Changchun spatially exhibited temperature increases (polygon in Fig. 15(E)). The reason for this was that the

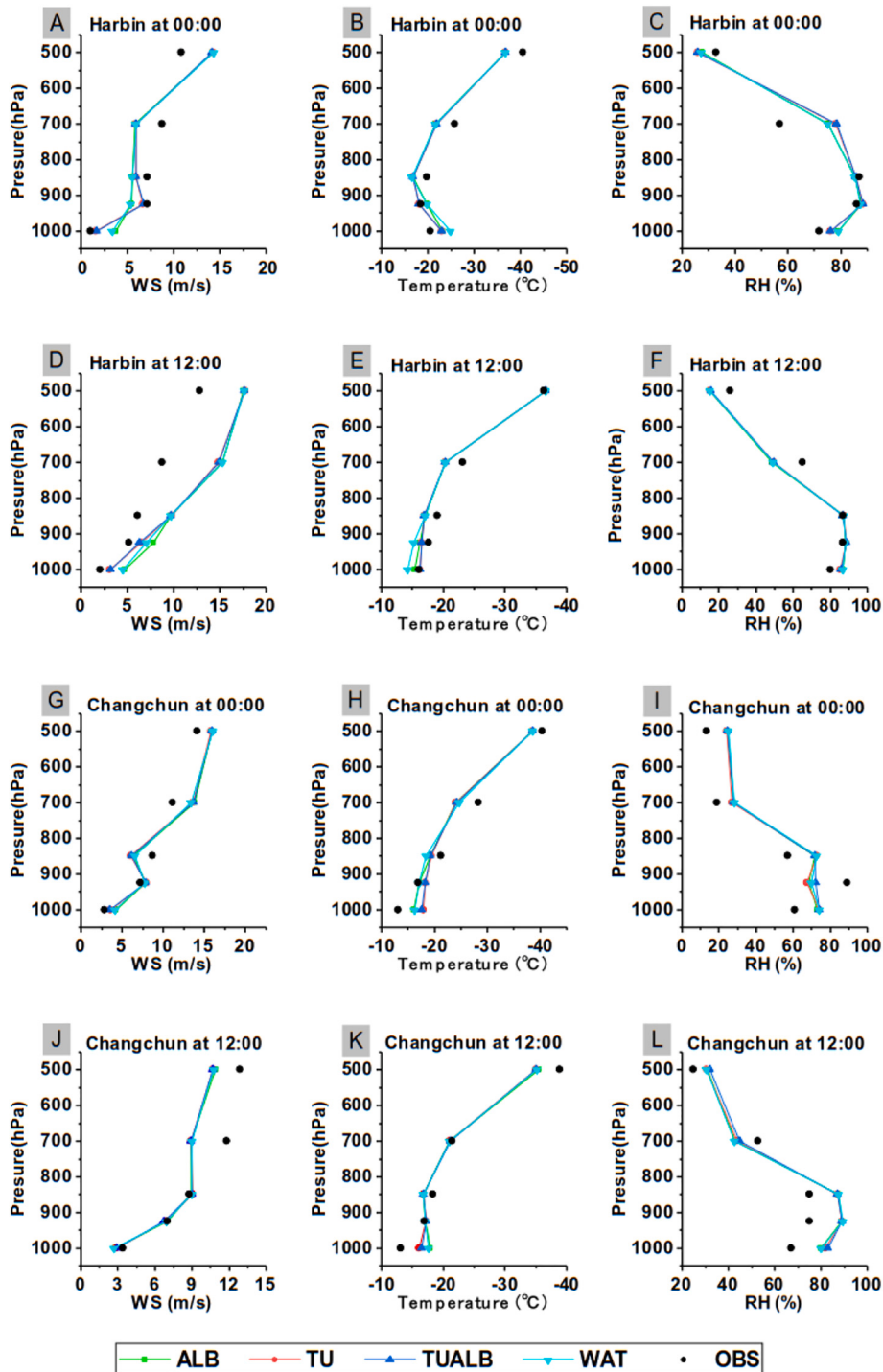


Fig. 11. Vertical profiles of simulated wind speed, temperature, relative humidity at Harbin and Changchun stations by the four scenarios with default AH parameters (color lines) against observations (black dots).

two regions were allocated more AH determined by a large population.

Fig. 16 illustrates the vertical cross section of mean temperature differences. Temperatures at the surface and lower atmosphere increased in most places along the transect with significant differences below the 600-m height over urban regions (Changchun $125.1^\circ \sim 125.5^\circ$, Harbin $126.5^\circ \sim 127.0^\circ$). This can be attributed to the change in the albedo that alters outgoing radiation flux, which in turn changes the surface energy balance including HFX and latent heat fluxes (Fig. S4). Lower albedo manifests that the underlying surface tends to absorb more heat, thereby increasing the surface air temperatures (Fig. 16(D)). In

addition, the air temperature showed increment over Harbin and Changchun as AH parameters updating, this might ascribe to the increase of heat fluxes as well.

4.4. Changes in relative humidity

RH2 differences between all “updated simulations” and WAT showed decreases, with the difference of -0.2% between ALB and WAT scenarios, -1.0% between TU and WAT scenarios, and -0.8% between TUALB and WAT scenarios. The RH in underlying surfaces showed a

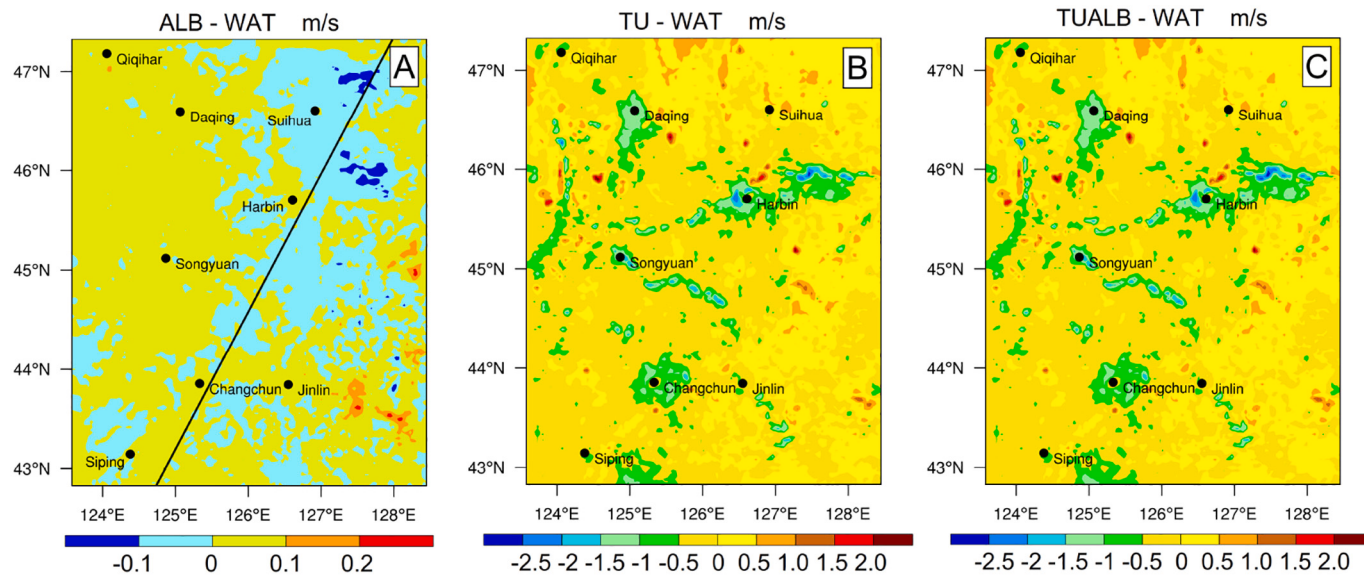


Fig. 12. Averaged wind speed difference in the horizontal direction. A- WS10_{ALB}-WAT, B- WS10_{TU}-WAT, C- WS10_{TUALB}-WAT. The black line in subplot A represents a vertical cross section, and the same for subsequent T2, RH2, and PBLH.

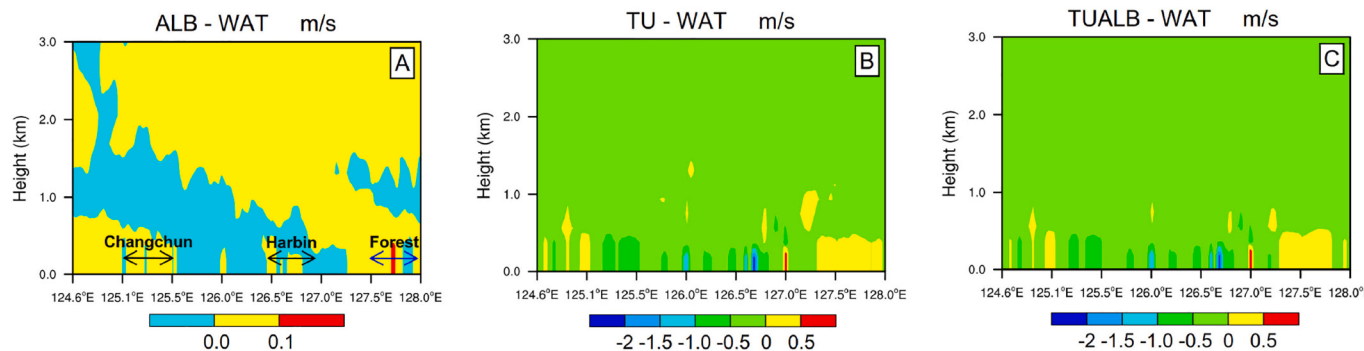


Fig. 13. A vertical cross section of averaged wind speed difference along the transect (black line in Fig. 12(A)). A- WS_{ALB}-WAT, B- WS_{TU}-WAT, C- WS_{TUALB}-WAT. The black lines with arrows in subplot A represent urban areas of Changchun and Harbin, the blue line with arrow represents the forest region, similarly hereafter.

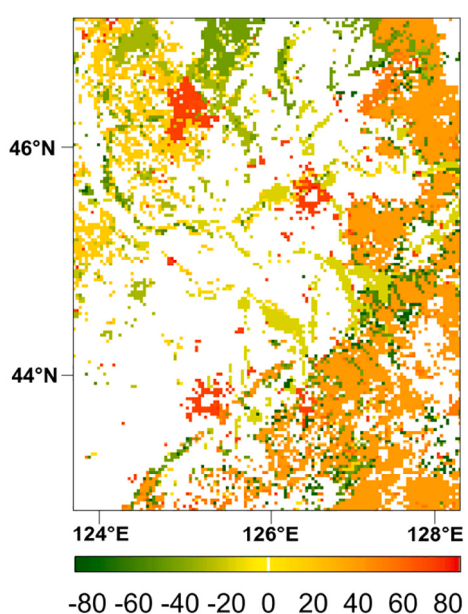


Fig. 14. The changes in surface roughness length by TU_{LC} minus USGS_{LC}.

negligible response to MSA and land cover changes (Fig. 17). Again, the new datasets tended to overestimate RH2 over water bodies. Likewise, RH differences in the lower atmosphere in the vertical cross sections also showed reductions as low as -0.5% ($RH_{ALB-WAT}$), -0.7% (RH_{TU-WAT}), and -0.6% ($RH_{TUALB-WAT}$) (Fig. 18). In other words, RH was less sensitive to MSA and land cover changes. One reason for this is mainly ascribed to changed soil moisture characteristics. In winter, in the presence of snow, frozen soil has adverse to the exchange of heat and moisture not only within the soil profile but also between the surface and overlying near-surface atmosphere. These factors are all prescribed in the Noah LSM which can otherwise affect the surface energy and water budget (Ek et al., 2003). Besides, the slight improvement was due to the differences in the planetary boundary layer schemes prescribed (Banks et al., 2016). The role of modifying tunable parameters is critical for simulation as well. Quan et al. (2016) investigated the model response to modified planetary boundary layer parameters like *Prandtl Number at the Top of the Surface Layer*, results indicated those parameters involved were shown sensitivity to relative humidity outputs evaluated. Here, the modeling was conducted by the default parameters, this may provide an important insight into localized physics schemes and parameters over China's cold region. Also, the result here is not in line with Zhu et al. (2017), who simulates a large RH difference over the Pearl River Delta region in January. Typically, the Pearl River Delta region is located in the Southern seaboard of the China Sea where there is no

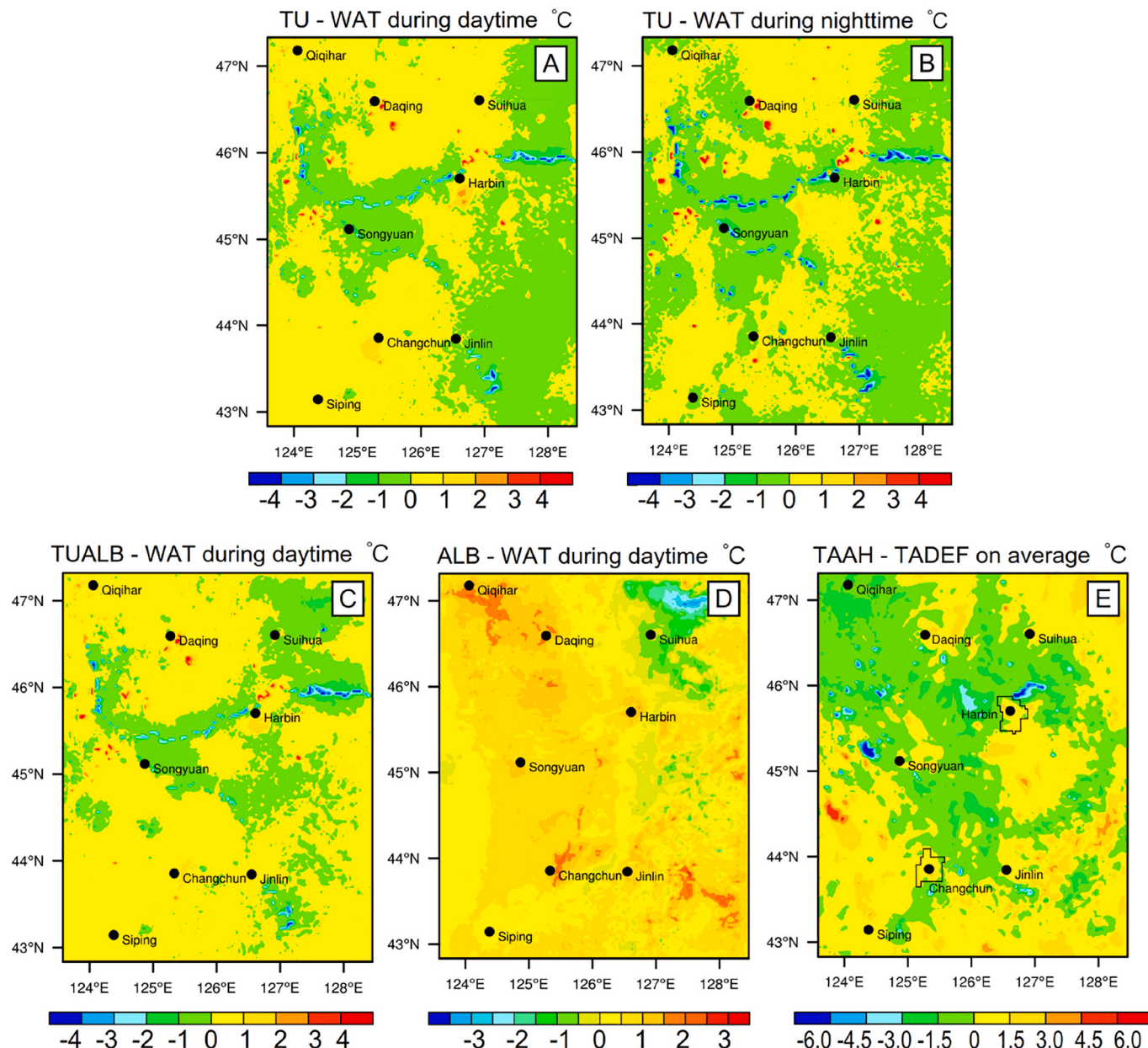


Fig. 15. T2 difference in the model domain. A, B- $T2_{TU\text{-}WAT}$ during daytime and nighttime, C- $T2_{TUALB\text{-}WAT}$ during daytime, D- $T2_{ALB\text{-}WAT}$ during daytime. E- $T2_{TAAH\text{-}TADEF}$ on average.

snow cover in winter at all, whereas the seasonal snow cover prevails in northeast China throughout the winter season. Also, the result is different from a previous study in which increasing snow albedo leads to a noticeable RH₂ increment over a valley region by Zhang and Pu (2019), this can be ascribed to terrain differences.

4.5. Changes in the planetary boundary layer heights

The mean PBLH differences between updated and default simulations are shown in Fig. 19. Positive differences could be observed in urban regions, agreeing with de la Paz et al. (2016). As mentioned previously, MSA exhibited a decreasing pattern over the study area, thereby affecting the surface energy budget and the structure and diurnal changes in the boundary layer (Ran et al., 2015). Potential implications in response to the new MSA dataset in PBLH modeling runs could be identified. The change of snow albedo can have an influence on net radiation fluxes (Fig. S5), and the varying sensible heat consequently

leads to evolution in the surface temperature and a varied PBLH. Thicker PBLH is spatially correlated with increasing roughness over the urban area as DCP switching into LIR/UBL. Diurnal PBLH changes across the sections were more significant at 06:00 and 18:00 LST, 2 January 2018 (Fig. 20). Higher PBLH were in ALB and TUALB than that in TU and WAT during the daytime, but almost no differences during the nighttime, primarily due to the stable boundary layer at night.

5. Conclusions

The “Harbin-Changchun megalopolis” located in the cold region of northeast China presents unique meteorological characteristics by snow-covered features and dramatic land cover transformation in recent years. Therefore, this paper explored the variations of WS, temperature, RH both horizontally and vertically in winter caused by changed MSA and land cover, according to four modeled scenarios by default and new geographical datasets. Also, difference in PBLH was evaluated. First of

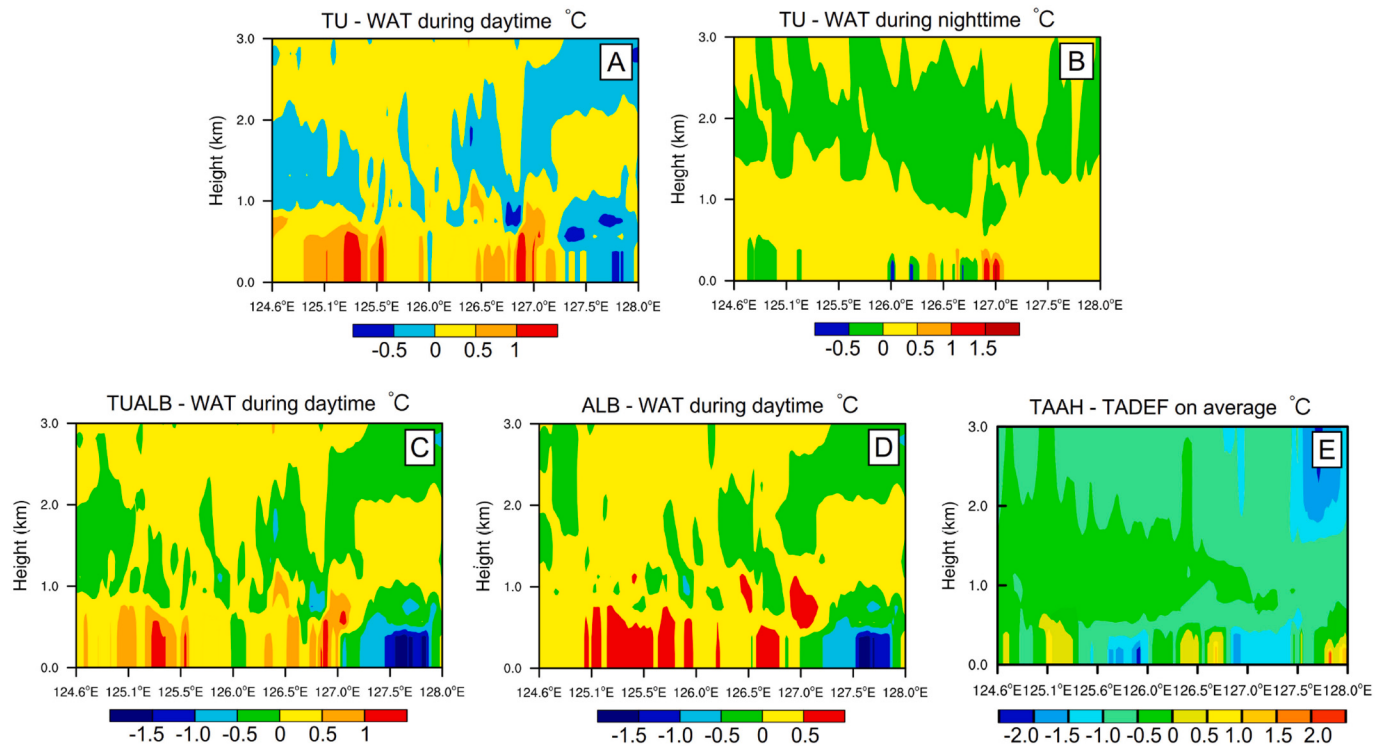


Fig. 16. Temperature difference in the vertical cross section. A- $T_{TU\text{-}WAT}$ during daytime, B- $T_{TU\text{-}WAT}$ during nighttime, C- $T_{TUALB\text{-}WAT}$ during daytime, D- $T_{ALB\text{-}WAT}$ during daytime, E- $T_{TAAH\text{-}TADEF}$ on average.

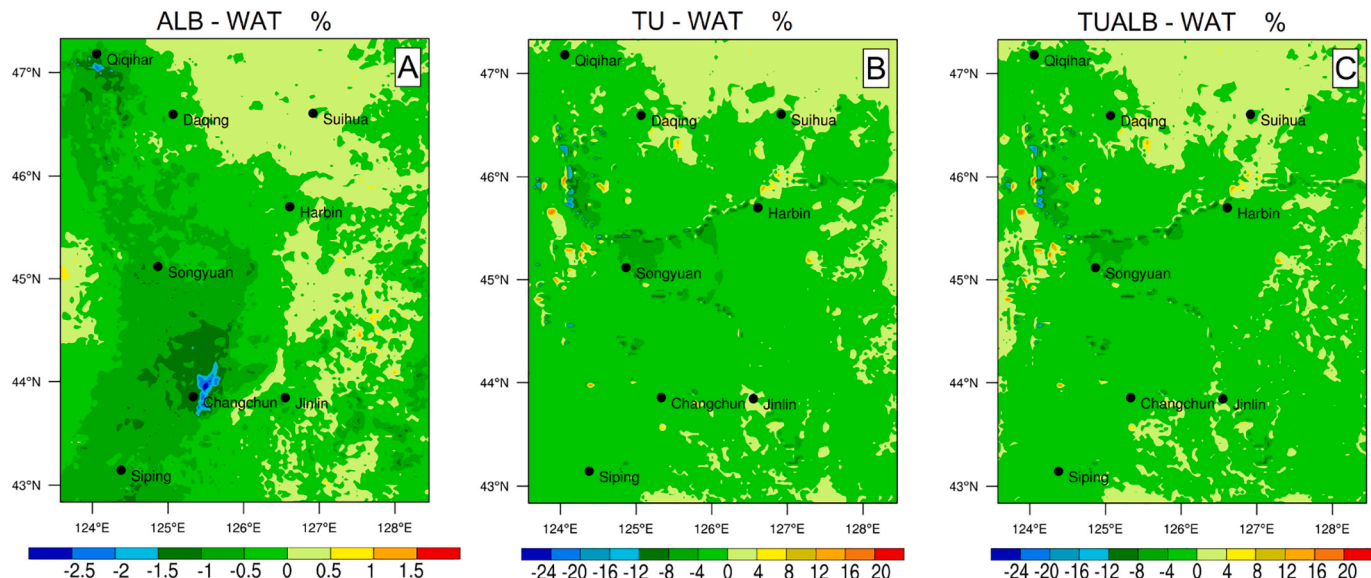


Fig. 17. Same as Fig. 12, but for 2-m relative humidity.

all, the high adaptability of the BNU_MSA and TU_LC has been proved but presents different effects for variables in comparison with observation. TU_LC favors WS10 simulation, yielding an identical improvement of 0.36 m/s by both TU and TUALB, while ALB by BNU_MSA updating performs the best on modeled PBLH. Both TU_LC and BNU_MSA play important role in T2 simulation.

Sensitivities of variables to changes of MSA and land cover over domain-wide are different and bear specific characteristics, depending on the locations where changes happen. Differences for WS10 are large in regions where the transformations of DCP to LIR (or UBL) and Mixed Forest to DBF occur, which illustrates the influence of changed surface

roughness length at the surface. In terms of vertical difference, larger variations always emerge in 600-m, also, these large variations are mainly confined within urban and forest regions. Noticeable changes are observed over urban and forest regions in both the horizontal and vertical directions where conversions from DCP to LIR and Mixed Forest to DBF happen. In terms of the influence of AH on temperature, TAAH generally shows underestimation, similar to those simulations by default AH parameters. However, the modified two parameters have a significant influence on T2 increment over the downtown big cities (Harbin and Changchun). Apart from these, simulated temperature possesses two regularities, first, the effects of MSA on temperature are comparable

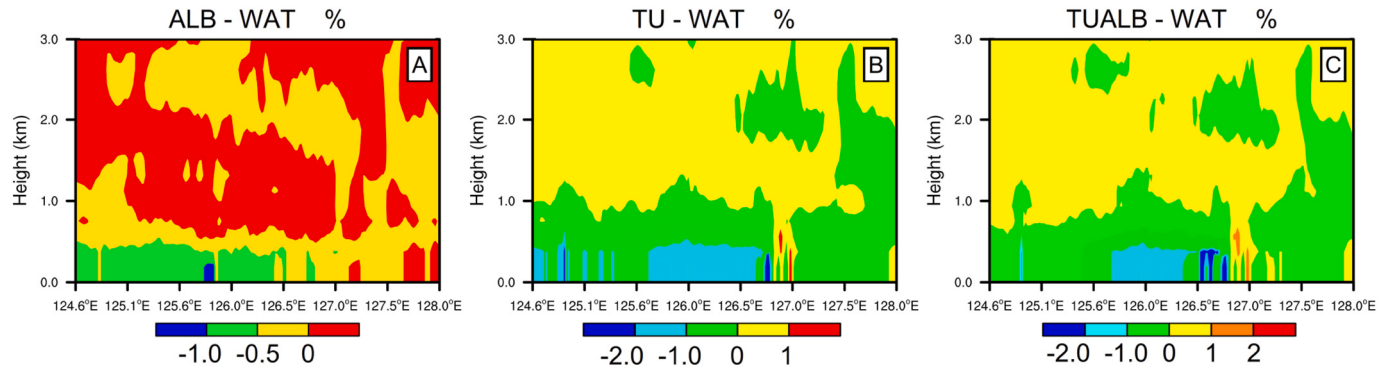


Fig. 18. Same as Fig. 13, but for relative humidity.

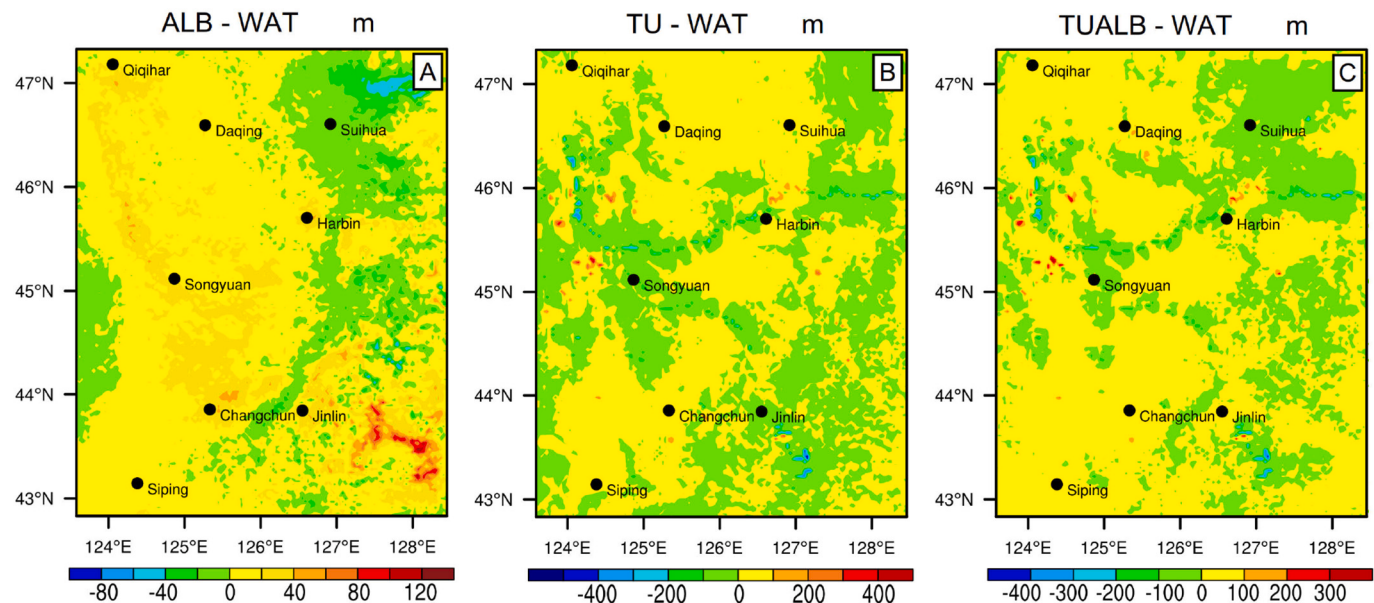


Fig. 19. Same as Fig. 12, but for PBLH.

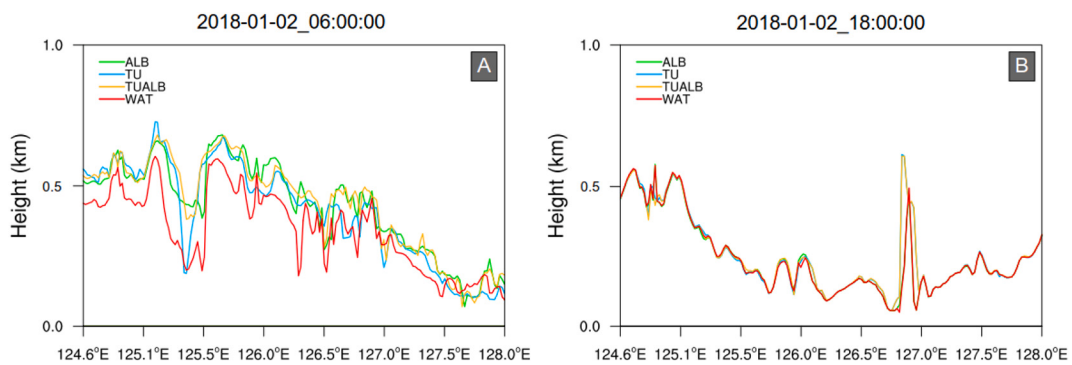


Fig. 20. Diurnal PBLH variations in different scenarios across the section at two given time points on January 2th, 2018. A, B- PBLH variations at 06:00 and 18:00.

to or larger in magnitude than that of land cover changes. Second, the impacts of water bodies related transformations, mainly sprawling into DCP, are overestimated during winter because it shares similar surface features with DCP in reality.

It can be verified that the MSA particularly plays an important role in PBLH simulation in the daytime because higher PBLH in ALB is observed, which is ascribed to the generally decreasing albedo over the study area can have a significant impact on the radiation condition and

consequently greatly influences the surface temperature, heat flux, and momentum transport. As for RH, changes in the horizontal and vertical directions in response to MSA and land cover are negligible. In general, the modeled variables are improved with the use of updated MSA and land cover datasets, and particularly, they are sensitive to the changes of MSA and land cover occurred over urban and forest regions during winter.

CRediT authorship contribution statement

Donglei Fu (Conceptualization, Data curation, Formal analysis, Investigation, Methodology, Software, Validation, Writing), Wei Zhang (Data curation, Software, Validation), Yanfeng Xing (Data curation, Resources), Haizhi Li (Data curation, Resources), Pengjie Wang (Data curation, Resources), Bo Li (Conceptualization, Formal analysis, Methodology, Software), Xiaofei Shi (Conceptualization, Formal analysis, Methodology, Software), Jinxiang Zuo (Data curation, Resources), Stephen Yabo (Formal analysis, Review & editing), Samit Thapa (Conceptualization, Methodology, Review & editing), Lu Lu (Methodology, Resources), Hong Qi (Conceptualization, Formal analysis, Funding acquisition, Methodology, Resources, Supervision, Validation, Review & editing), Jianmin Ma (Formal analysis, Methodology, Resources, Validation, Review & editing).

Declaration of Competing Interest

None.

Acknowledgement

The land cover dataset developed by Tsinghua University and the albedo production from Beijing Normal University are downloaded from <http://www.geodata.cn>. We thank the Global Data Assimilation System (GDAS) provides FNL forcing data (https://rda.ucar.edu/data_sets/ds083.2/index.html#sfol-wl/data/ds083.2?g=2). The observational data including ground station, sounding station, and laser radar data are obtained from China Meteorological Data Service Center (http://www.nmic.cn/dataService/cdcindex/datacode/A.0012.0001/show_value/normal.html), University of Wyoming (<http://www.weather.uwyo.edu/upperair/sounding.html>), and Heilongjiang Provincial Environmental Monitoring Center. The snow equivalent water data are download from <http://www.globsnow.info/swe/nrt/>. We state that samples of methods for data processing, NCL scripts for the plot, and the processed data (including shapefile, raster, NETCDF, etc) are accessible to Mendeley Data Repository <https://data.mendeley.com/datasets/k7t3mrcm68/draft?a=a1b1ff94-bb46-407d-905f-2fefb8e7ce6f>. This work was supported by the State Key Laboratory of Urban Water Resource and Environment (Harbin Institute of Technology) (No. 2018TS01).

Appendix A. Supplementary data

Supplementary data to this article can be found online at <https://doi.org/10.1016/j.atmosres.2021.105449>.

References

- Acs, F., Gyoengyoesi, A.Z., Breuer, H., Horvath, A., Mona, T., Rajkai, K., 2014. Sensitivity of WRF-simulated planetary boundary layer height to land cover and soil changes. *Meteorol. Z.* 23 (3), 279–293. <https://doi.org/10.1127/0941-2948/2014/0544>.
- Azhdari, A., Soltani, A., Alidadi, M., 2018. Urban morphology and landscape structure effect on land surface temperature: evidence from Shiraz, a semi-arid city. *Sustain. Cities Soc.* 41, 853–864. <https://doi.org/10.1016/j.scs.2018.06.034>.
- Banks, R.F., Tiana-Alsina, J., Baldasano, J.M., Rocadenbosch, F., Papayannis, A., Solomos, S., Tzanis, C.G., 2016. Sensitivity of boundary-layer variables to PBL schemes in the WRF model based on surface meteorological observations, lidar, and radiosondes during the Hygra-CD campaign. *Atmos. Res.* 176, 185–201. <https://doi.org/10.1016/j.atmosres.2016.02.024>.
- Barlage, M., Zeng, X.B., Wei, H.L., Mitchell, K.E., 2005. A global 0.05 degrees maximum albedo dataset of snow-covered land based on MODIS observations. *Geophys. Res. Lett.* 32 (17), 1–5. <https://doi.org/10.1029/2005gl022881>.
- Betts, A.K., Ball, J.H., Beljaars, A.C.M., Miller, M.J., Viterbo, P.A., 1996. The land surface-atmosphere interaction: a review based on observational and global modeling perspectives. *J. Geophys. Res. Atmos.* 101 (D3), 7209–7225. <https://doi.org/10.1029/95jd02135>.
- Carvalho, D., Rocha, A., Gomez-Gesteira, M., Santos, C., 2012. A sensitivity study of the WRF model in wind simulation for an area of high wind energy. *Environ. Model. Softw.* 33, 23–34. <https://doi.org/10.1016/j.envsoft.2012.01.019>.
- Cermak, V., Bodri, L., Kresl, M., Dedecek, P., Safanda, J., 2017. Eleven years of ground-air temperature tracking over different land cover types. *Int. J. Climatol.* 37 (2), 1084–1099. <https://doi.org/10.1002/joc.4764>.
- Chen, F., Dudhia, J., 2001. Coupling an advanced land surface-hydrology model with the Penn State-NCAR MM5 modeling system. Part I: model implementation and sensitivity. *Mon. Weather Rev.* 129 (4), 569–585. [https://doi.org/10.1175/1520-0493\(2001\)129<0569:Caalsh>2.0.Co;2](https://doi.org/10.1175/1520-0493(2001)129<0569:Caalsh>2.0.Co;2).
- Chen, D., Lu, D.R., Chen, Z.Y., 2014. Simulation of the stratosphere-troposphere exchange process in a typical cold vortex over Northeast China. *Sci. China Earth Sci.* 57 (7), 1452–1463. <https://doi.org/10.1007/s11430-014-4864-x>.
- De Meij, A., Vinuesa, J.F., 2014. Impact of SRTM and Corine Land Cover data on meteorological parameters using WRF. *Atmos. Res.* 143, 351–370. <https://doi.org/10.1016/j.atmosres.2014.03.004>.
- De Meij, A., Bossoli, E., Penard, C., Vinuesa, J.F., Price, I., 2015. The effect of SRTM and Corine Land Cover data on calculated gas and PM10 concentrations in WRF-Chem. *Atmos. Environ.* 101, 177–193. <https://doi.org/10.1016/j.atmosenv.2014.11.033>.
- DuVivier, A.K., Cassano, J.J., 2013. Evaluation of WRF model resolution on simulated mesoscale winds and surface fluxes near Greenland. *Mon. Weather Rev.* 141 (3), 941–963. <https://doi.org/10.1175/mwr-d-12-00091.1>.
- Ek, M.B., Mitchell, K.E., Lin, Y., Rogers, E., Grunmann, P., Koren, V., Gayno, G., Tarpley, J.D., 2003. Implementation of Noah land surface model advances in the National Centers for Environmental Prediction operational mesoscale Eta model. *J. Geophys. Res. Atmos.* 108 (D22). <https://doi.org/10.1029/2002jd003296>.
- Fang, L., Zhan, X.W., Hain, C.R., Yin, J.F., Liu, J.C., 2018. Impact of GVF derivation methods on Noah land surface model simulations and WRF model forecasts. *J. Hydrometeorol.* 19 (12), 1917–1933. <https://doi.org/10.1175/jhm-d-18-0075.1>.
- Friedl, M.A., McIver, D.K., Hodges, J.C.F., Zhang, X.Y., Muchoney, D., Strahler, A.H., Woodcock, C.E., Gopal, S., Schneider, A., Cooper, A., 2002. Global land cover mapping from MODIS: algorithms and early results. *Remote Sens. Environ.* 83 (1–2), 287–302. [https://doi.org/10.1016/s0034-4257\(02\)00078-0](https://doi.org/10.1016/s0034-4257(02)00078-0).
- Friedl, M.A., Sulla-Menashe, D., Tan, B., Schneider, A., Ramankutty, N., Sibley, A., Huang, X.M., 2010. MODIS Collection 5 global land cover: Algorithm refinements and characterization of new datasets. *Remote. Sens. Environ.* 114 (1), 168–182. <https://doi.org/10.1016/j.rse.2009.08.016>.
- Fu, Q., Peng, L., Li, T.X., Cui, S., Liu, D., Yan, P.R., Chen, H.G., 2019. Analysis of characteristic snow parameters and associated factors in a cold region in northeast China. *Water Sci. Technol. Water Supply* 19 (2), 511–518. <https://doi.org/10.2166/ws.2018.096>.
- Gao, H., Jia, G.S., 2013. Assessing disagreement and tolerance of misclassification of satellite-derived land cover products used in WRF model applications. *Adv. Atmos. Sci.* 30 (1), 125–141. <https://doi.org/10.1007/s00376-012-2037-4>.
- Gong, P., 2009. Accuracy test of global land cover map based on Global Flux Observation Station. *Prog. Nat. Sci.* 19 (7), 754–759.
- Hirsch, A.L., Pitman, A.J., Kala, J., 2014. The role of land cover change in modulating the soil moisture-temperature land-atmosphere coupling strength over Australia. *Geophys. Res. Lett.* 41 (16), 5883–5890. <https://doi.org/10.1002/2014gl061179>.
- Ioannidou, L., Yu, W., Belair, S., 2014. Forecasting of surface winds over eastern Canada using the Canadian offline land surface modeling system. *J. Appl. Meteorol. Climatol.* 53 (7), 1760–1774. <https://doi.org/10.1175/jamc-d-12-0284.1>.
- Jimenez, P.A., Dudhia, J., Gonzalez-Rouco, J.F., Navarro, J., Montavez, J.P., Garcia-Bustamante, E., 2012. A revised scheme for the WRF surface layer formulation. *Mon. Weather Rev.* 140 (3), 898–918. <https://doi.org/10.1175/mwr-d-11-00056.1>.
- Jimenez-Esteve, B., Udina, M., Soler, M.R., Pepin, N., Miro, J.R., 2018. Land use and topography influence in a complex terrain area: a high resolution mesoscale modelling study over the Eastern Pyrenees using the WRF model. *Atmos. Res.* 202, 49–62. <https://doi.org/10.1016/j.atmosres.2017.11.012>.
- Kuik, F., Lauer, A., Churkina, G., Van der Gon, H.A.C.D., Fenner, D., Mar, K.A., Butler, T.M., 2016. Air quality modelling in the Berlin-Brandenburg region using WRF-Chem v3.7.1: sensitivity to resolution of model grid and input data. *Geosci. Model Dev.* 9 (12), 4339–4363. <https://doi.org/10.5194/gmd-9-4339-2016>.
- Kumar, S.V., Peters-Lidard, C.D., Eastman, J.L., Tao, W.K., 2008. An integrated high-resolution hydrometeorological modeling testbed using LIS and WRF. *Environ. Model. Softw.* 23 (2), 169–181. <https://doi.org/10.1016/j.envsoft.2007.05.012>.
- Kurkowski, N.P., Stensrud, D.J., Baldwin, M.E., 2003. Assessment of implementing satellite-derived land cover data in the Eta model. *Weather Forecast.* 18 (3), 404–416. [https://doi.org/10.1175/1520-0434\(2003\)18<404:Aoisd>2.0.Co;2](https://doi.org/10.1175/1520-0434(2003)18<404:Aoisd>2.0.Co;2).
- Lee, S.H., Lee, H., Park, S.B., Woo, J.W., Lee, D.I., Baik, J.J., 2016. Impacts of in-canyon vegetation and canyon aspect ratio on the thermal environment of street canyons: numerical investigation using a coupled WRF-VUCM model. *Q. J. Roy. Meteor. Soc.* 142 (699), 2562–2578. <https://doi.org/10.1002/qj.2847>.
- Li, M.M., Wang, T.J., Xie, M., Zhuang, B.L., Li, S., Han, Y., Song, Y., Cheng, N.L., 2017. Improved meteorology and ozone air quality simulations using MODIS land surface parameters in the Yangtze River Delta urban cluster, China. *J. Geophys. Res. Atmos.* 122 (5), 3116–3140. <https://doi.org/10.1002/2016jd026182>.
- Li, J.Y., Zheng, X.Q., Zhang, C.X., Chen, Y.M., 2018a. Impact of land-use and land-cover change on meteorology in the Beijing-Tianjin-Hebei region from 1990 to 2010. *Sustainability* 10 (1). <https://doi.org/10.3390/su10010176>.
- Li, X., Wu, J.R., Elser, M., Feng, T., Cao, J.J., El-Haddad, I., Huang, R.J., Tie, X.X., Prevot, A.S.H., Li, G.H., 2018b. Contributions of residential coal combustion to the air quality in Beijing-Tianjin-Hebei (BTH), China: a case study. *Atmos. Chem. Phys.* 18 (14), 10675–10691. <https://doi.org/10.5194/acp-18-10675-2018>.
- Li, Z.G., Lyu, S.H., Wen, L.J., Zhao, L., Meng, X.H., Ao, Y.H., 2018c. Effect of roughness lengths on surface energy and the planetary boundary layer height over high-altitude Ngoring Lake. *Theor. Appl. Climatol.* 133 (3–4), 1191–1205. <https://doi.org/10.1007/s00704-017-2258-7>.

- Liao, J.B., Wang, T.J., Wang, X.M., Xie, M., Jiang, Z.Q., Huang, X.X., Zhu, J.L., 2014. Impacts of different urban canopy schemes in WRF/Chem on regional climate and air quality in Yangtze River Delta, China. *Atmos. Res.* 145, 226–243. <https://doi.org/10.1016/j.atmosres.2014.04.005>.
- Liu, N.F., Liu, Q., Wang, L.Z., Liang, S.L., Wen, J.G., Qu, Y., Liu, S.H., 2013. A statistics-based temporal filter algorithm to map spatiotemporally continuous shortwave albedo from MODIS data. *Hydrol. Earth. Syst. Sci.* 17 (6), 2121–2129. <https://doi.org/10.5194/hess-17-2121-2013>.
- Tu, T.X., Zhang, S.W., Yu, L.X., Bu, K., Yang, J.C., Chang, L.P., 2017. Simulation of regional temperature change effect of land cover change in agroforestry ecotone of Neijiang River Basin in China. *Theor. Appl. Climatol.* 128 (3–4), 971–981. <https://doi.org/10.1007/s00704-016-1750-9>.
- Loveland, T.R., Merchant, J.W., Merchant, J.F.C., Ohlen, D.O., Reed, B.C., Olson, P., Hutchinson, J., 1995. Seasonal Land-Cover Regions of the United States, 85(2), pp. 339–355. <https://doi.org/10.1111/j.1467-8306.1995.tb01797.x-11>.
- Massad, R.S., Lathiere, J., Strada, S., Perrin, M., Personne, E., Stefanon, M., Stella, P., Szopa, S., de Noblet-Ducoudre, N., 2019. Reviews and syntheses: influences of landscape structure and land uses on local to regional climate and air quality. *Biogeosciences* 16 (11), 2369–2408. <https://doi.org/10.5194/bg-16-2369-2019>.
- Oaida, C.M., Xue, Y.K., Flanner, M.G., Skiles, S.M., De Sales, F., Painter, T.H., 2015. Improving snow albedo processes in WRF/SSIB regional climate model to assess impact of dust and black carbon in snow on surface energy balance and hydrology over western US. *J. Geophys. Res. Atmos.* 120 (8), 3228–3248. <https://doi.org/10.1002/2014jd022444>.
- Ooi, M.C.G., Chan, A., Ashfold, M.J., Oozer, M.Y., Morris, K.I., Kong, S.S.K., 2019. The role of land use on the local climate and air quality during calm inter-monsoon in a tropical city. *Geosci. Front.* 10 (2), 405–415. <https://doi.org/10.1016/j.gsf.2018.04.005>.
- Pan, X.D., Li, X., Cheng, G.D., Chen, R.S., Hsu, K.L., 2017. Impact analysis of climate change on snow over a complex mountainous region using weather research and forecast model (WRF) simulation and MODERATE RESOLUTION IMAGING SPECTRORADIOMETER DATA (MODIS)-terra fractional snow cover products. *Remote Sens.* 9 (8) <https://doi.org/10.3390/rs9080774>.
- de la Paz, D., Borge, R., Martilli, A., 2016. Assessment of a high resolution annual WRF-BEP/CMAQ simulation for the urban area of Madrid (Spain). *Atmos. Environ.* 144, 282–296. <https://doi.org/10.1016/j.atmosenv.2016.08.082>.
- Qian, Y., Gustafson, W.I., Leung, L.R., Ghan, S.J., 2009. Effects of soot-induced snow albedo change on snowpack and hydrological cycle in western United States based on Weather Research and Forecasting chemistry and regional climate simulations. *J. Geophys. Res. Atmos.* 114 (D03) <https://doi.org/10.1029/2008jd011039>.
- Quan, J.P., Di, Z.H., Duan, Q.Y., Gong, W., Wang, C., Gan, Y.J., Ye, A.Z., Miao, C.Y., 2016. An evaluation of parametric sensitivities of different meteorological variables simulated by the WRF model. *Q. J. R. Meteorol. Soc.* 142 (700), 2925–2934. <https://doi.org/10.1002/qj.2885>.
- Ran, L.M., Gilliam, R., Binkowski, F.S., Xiu, A.J., Pleim, J., Band, L., 2015. Sensitivity of the Weather Research and Forecast/Community Multiscale Air Quality modeling system to MODIS LAI, FPAR, and albedo. *J. Geophys. Res. Atmos.* 120 (16), 8491–8511. <https://doi.org/10.1002/2015jd023424>.
- Santos-Alamillos, F.J., Pozo-Vazquez, D., Ruiz-Arias, J.A., Tovar-Pescador, J., 2015. Influence of land-use misrepresentation on the accuracy of WRF wind estimates: Evaluation of GLCC and CORINE land-use maps in southern Spain. *Atmos. Res.* 157, 17–28. <https://doi.org/10.1016/j.atmosres.2015.01.006>.
- Schicker, I., Arias, D.A., Seibert, P., 2016. Influences of updated land-use datasets on WRF simulations for two Austrian regions. *Meteorol. Atmos. Phys.* 128 (3), 279–301. <https://doi.org/10.1007/s00703-015-0416-y>.
- Sertel, E., Robock, A., Ormeci, C., 2010. Impacts of land cover data quality on regional climate simulations. *Int. J. Climatol.* 30 (13), 1942–1953. <https://doi.org/10.1002/joc.2036>.
- Srinivas, C.V., Rao, D.V.B., Prasad, D.H., Hari Prasad, K.B.R.R., Baskaran, R., Venkatraman, B., 2015. A study on the influence of the land surface processes on the southwest monsoon simulations using a regional climate model. *Pure Appl. Geophys.* 172 (10), 2791–2811. <https://doi.org/10.1007/s00024-014-0905-9>.
- Tao, Z., Santanello, J.A., Chin, M., Zhou, S., Tan, Q., Kemp, E.M., Peters-Lidard, C.D., 2013. Effect of land cover on atmospheric processes and air quality over the continental United States - a NASA Unified WRF (NU-WRF) model study. *Atmos. Chem. Phys.* 13 (13), 6207–6226. <https://doi.org/10.5194/acp-13-6207-2013>.
- Thomas, L., Dash, S.K., Mohanty, U.C., Babu, C.A., 2018. Features of western disturbances simulated over north India using different land-use data sets. *Meteorol. Appl.* 25 (2), 246–253. <https://doi.org/10.1002/met.1687>.
- Touchaei, A.G., Akbari, H., Tessum, C.W., 2016. Effect of increasing urban albedo on meteorology and air quality of Montreal (Canada) - episodic simulation of heat wave in 2005. *Atmos. Environ.* 132, 188–206. <https://doi.org/10.1016/j.atmosenv.2016.02.033>.
- Toure, A.A., Tidjani, A.D., Rajot, J.L., Marticorena, B., Bergametti, G., Bouet, C., Ambouta, K.J.M., Garba, Z., 2019. Dynamics of wind erosion and impact of vegetation cover and land use in the Sahel: a case study on sandy dunes in southeastern Niger. *Catena* 177, 272–285. <https://doi.org/10.1016/j.catena.2019.02.011>.
- Trlica, A., Hutyra, L.R., Schaaf, C.L., Erb, A., Wang, J.A., 2017. Albedo, land cover, and daytime surface temperature variation across an urbanized landscape. *Earths Fut.* 5 (11), 1084–1101. <https://doi.org/10.1002/2017ef000569>.
- Wang, S.Z., Sun, B., 2018. The impacts of different land surface parameterization schemes on Northeast China snowfall simulation. *Meteorol. Atmos. Phys.* 130 (5), 583–590. <https://doi.org/10.1007/s00703-017-0539-4>.
- Wang, Z.M., Wang, X.M., 2011. Estimation and sensitivity test of anthropogenic heat flux in Guangzhou. *J. Meteorol. Sci.* 31 (4), 422–430 (in Chinese).
- Wang, H.J., Yu, E.T., Yang, S., 2011. An exceptionally heavy snowfall in Northeast China: large-scale circulation anomalies and hindcast of the NCAR WRF model. *Meteorol. Atmos. Phys.* 113 (1–2), 11–25. <https://doi.org/10.1007/s00703-011-0147-7>.
- Wang, M.N., Xiong, Z., Yan, X.D., 2015. Modeling the climatic effects of the land use/cover change in eastern China. *Phys. Chem. Earth* 87–88, 97–107. <https://doi.org/10.1016/j.pce.2015.07.009>.
- Wen, X.H., Lu, S.H., Jin, J.M., 2012. Integrating remote sensing data with WRF for improved simulations of Oasis effects on local weather processes over an Arid region in northwestern China. *J. Hydrometeorol.* 13 (2), 573–587. <https://doi.org/10.1175/jhm-d-10-05001.1>.
- Wen, X.H., Liao, X.H., Yuan, W.P., Yan, X.D., Wei, Z.G., Liu, H.Z., Feng, J.M., Lu, S.H., Dong, W.J., 2014. Numerical simulation and data assimilation of the water-energy cycle over semiarid northeastern China. *Sci. China Earth Sci.* 57 (10), 2340–2356. <https://doi.org/10.1007/s11430-014-4914-4>.
- Yang, Y.K., Xiao, P.F., Feng, X.Z., Li, H.X., 2017. Accuracy assessment of seven global land cover databases over China. *ISPRS. J. Photogramm.* 125, 156–173. <https://doi.org/10.1016/j.isprsjprs.2017.01.016>.
- Yu, M., Carmichael, G.R., Zhu, T., Cheng, Y.F., 2012. Sensitivity of predicted pollutant levels to urbanization in China. *Atmos. Environ.* 60 (none), 544–554. <https://doi.org/10.1016/j.atmosenv.2012.06.075>.
- Yu, L.X., Liu, T.X., Bu, K., Yang, J.C., Chang, L.P., Zhang, S.W., 2017. Influence of snow cover changes on surface radiation and heat balance based on the WRF model. *Theor. Appl. Climatol.* 130 (1–2), 205–215. <https://doi.org/10.1007/s00704-016-1856-0>.
- Zahra, J., Hashem, A., 2018. The effect of increasing surface albedo on urban climate and air quality: a detailed study for Sacramento, Houston, and Chicago. *Climate* 6 (2). <https://doi.org/10.3390/cli6020019>.
- Zhang, F.M., Pu, Z.X., 2019. Sensitivity of numerical simulations of near-surface atmospheric conditions to snow depth and surface Albedo during an ice fog event over Heber valley. *J. Appl. Meteorol. Climatol.* 58 (4), 797–811. <https://doi.org/10.1175/jamc-d-18-0064.1>.
- Zhu, K.G., Xie, M., Wang, T.J., Cai, J.X., Li, S.B., 2017. A modeling study on the effect of urban land surface forcing to regional meteorology and air quality over South China. *Atmos. Environ.* 152, 389–404. <https://doi.org/10.1016/j.atmosenv.2016.12.053>.